Control Design for Grid and Energy/Balancing Controllers of Modular Multilevel Converter Based VSC HVDC Systems

Christoph Hahn, *Member, IEEE,* Matthias Burkhardt, Matthias Luther, *Member, IEEE*
Institute of Electrical Energy Systems
Friedrich-Alexander-University of Erlangen-Nuremberg (FAU)
Erlangen, Germany
christoph.hahn@fau.de, matthias.burkhardt@fau.de, matthias.luther@fau.de

***Abstract*—This paper provides a comprehensive control design approach for Modular Multilevel Converter (MMC) based Voltage Source Converter (VSC) High-Voltage Direct Current (HVDC) systems. Detailed control design strategies for power, voltage, energy and horizontal/vertical balancing controllers, as well as their subordinated current controllers, are carried out using the approaches of symmetrical and amplitude optimum respectively. Furthermore, the design of the filters for the balancing controllers is revealed. An energization and start-up process of the HVDC system is presented; subsequently, a power reversal process is performed and an AC voltage drop is applied in order to verify the accuracy and stability of the proposed control strategy and to illustrate the dynamic behavior of the investigated HVDC system. It is shown that the appropriate control design guarantees the stability of the HVDC system during the entire range of operation.**

***Keywords*—Converter Control Design; Energy Balancing; Horizontal Balancing Control; High-Voltage Direct Current (HVDC); Modular Multilevel Converter (MMC); Amplitude Optimum; Symmetrical Optimum; Vertical Balancing Control.**

I. INTRODUCTION

The desire to use MMC VSC HVDC systems – firstly introduced from Lesnicar and Marquardt in 2003 [1] – has gained a lot of interest in Germany due to the German Grid Development Plan [2]. In order to transport the high amount of renewable energy from the northern part of Germany to the load centers in the south, HVDC solutions with a transmission capacity of approximately 6 to 8 GW are required. MMC VSC technology is the key component in pan-European grid enhancement plans, as depicted in ENTSO-E's Ten Year Network Development Plan [3]; it shows that numerous subsea cable connections are required for the integration of offshore windfarms and the elimination of transmission bottlenecks.

Particular distinguishing features of the MMC VSC technology are independent control of active and reactive power, low harmonic distortion due to the high amount of submodules and therefore, less space requirements in comparison to Line Commutated Converters (LCC), where AC and DC filters with a large footprint have to be applied. Moreover, black-start and fault-ride-through capabilities are noteworthy in terms of grid support in contrast to LCC based systems [4], [5]. Due to these facts, the MMC VSC technology is also the preferred solution for the connection of offshore windfarms.

EMT models of symmetrical monopole VSC HVDC systems with MMC technology are presented in [6] - [9]. Distributed capacitors are the key component of the MMC and studies concerning MMC capacitor voltage balancing control are published in [10] - [12]. Since Multi terminal (MT) networks will play an important role in the future, possible MT topologies are evaluated in [13]. A detailed review about MMC technology can be found in [14]. Nevertheless, an approach for the setting of the most important controllers of the system is still missing.

This paper presents a comprehensive control structure of the MMC VSC HVDC system and a detailed control design approach for those controllers; which includes the P/Q and V_{DC}/Q control with a subordinated i_{Nd}/i_{Nq} controller in order to exchange active and reactive power with the connected AC grids. Additionally, an energy controller as well as a horizontal and vertical balancing/symmetry controller with a subordinated $i_{diff\alpha}/i_{diff\beta}/i_{diff0}$ controller is used, in order to ensure the right amount of energy in the converter, as well as the accurate distribution of the energy in-between the converter arms. The superposition of these controllers as well as the control design using the approaches of amplitude optimum and symmetrical optimum are carried out.

After passive pre-charging via the adjacent AC grids, a subsequent start-up process of the HVDC system with the corresponding controllers is presented. Afterwards, a power reversal process of the system is performed, and subsequently AC voltage drops are applied. The stable dynamic behavior and the accuracy of the entire control system are evaluated.

Following Section I, the investigated MMC-HVDC system is described in Section II. Section III gives a detailed overview on the deployed control strategy; it is subdivided into two parts: Firstly the grid current controller and its respective outer control loops – comprising the P/Q and V_{DC}/Q controller – are presented. Consequently, the inner converter control is revealed; it compromises a subordinated current controller and the super-ordinated energy and balancing controllers. Section IV shows the simulation results.

II. EMT HVDC MODEL

The equivalent circuit diagram of the HVDC system is shown in Figure 1. As the number of submodules exceeds several hundred per converter arm, the series connection of half bridge

978-1-5090-1815-4/16/$31.00 ©2016 IEEE

or full bridge submodules are modeled with controlled voltage sources $v_{x,y,z}$; the adjacent AC grids are represented by a three phase voltage source $v_{x,y}$ and its appropriate grid reactance $L_{N,y}$, where $x \in \{a,b,c\}$, $y \in \{1,2\}$ and $z \in \{p,n\}$.

As shown in Figure 1, each converter comprises six converter arms, three positive and three negative ones; one converter arm contains a certain amount of submodules and a converter arm impedance. Z_{arm} is composed of an arm reactance L_{arm} and an equivalent arm resistance R_{arm}. Z_{DC} and C_{DC} represent the DC line. For reasons of clearness, the high ohmic DC grounding resistors are not depicted in detail.

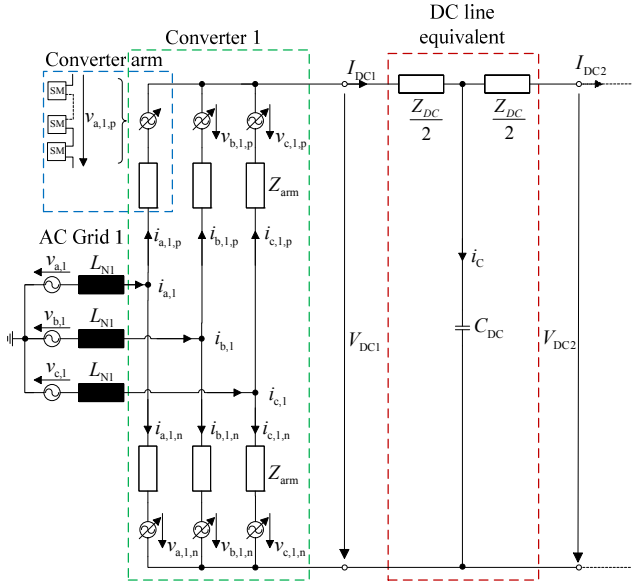

Figure 1: Equivalent circuit diagram of one converter of the MMC VSC HVDC system

Taking into account that each submodule and its respective Insulated Gate Bipolar Transistors (IGBT) can only be controlled with a sufficient voltage supply, an uncontrolled energization process has to be performed. Therefore, all submodules are blocked and each submodule capacitor is either bypassed or charged via its respective free-wheeling diode, see Figure 2.

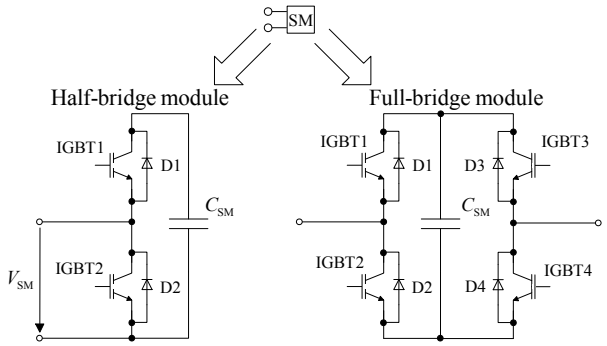

Figure 2: Submodule configuration

In the following, half-bridge submodules are deployed and the capacitors are solely charged during the positive half-cycle. During uncontrolled/passive pre-charging the submodule voltage reveals as follows:

$$\begin{aligned} v_{SM,x,y,z} &= \int \frac{n_{SM}}{C_{SM}} i_{x,y,z}\,\mathrm{d}t: \quad i_{x,y,z} > 0, \\ v_{SM,x,y,z} &= 0: \qquad\qquad\quad i_{x,y,z} < 0. \end{aligned} \tag{1}$$

In order to limit the AC currents, pre-charging resistors are applied. After pre-charging is completed the IGBTs can be switched properly.

As the series connection of submodules in one converter arm is modeled as a controlled voltage source, the submodule voltage has to be determined. In order to achieve an equal energy distribution among the submodules of one converter arm, a certain switching pattern has to be applied to the involved submodules. Detailed analyses about this are presented in [15]. However, once an equal distribution of the energy over the entire converter arm is assumed, the average submodule voltage can be derived:

$$\begin{aligned} E_{arm,x,y,z} &= \int v_{x,y,z} i_{x,y,z}\,\mathrm{d}t = n_{SM} E_{SM,x,y,z} = n_{SM} \frac{1}{2} C_{SM} v_{SM,x,y,z}^2, \\ \rightarrow v_{SM,x,y,z} &= \sqrt{\frac{2}{n_{SM} C_{SM}} \int v_{x,y,z} i_{x,y,z}\,\mathrm{d}t}. \end{aligned} \tag{2}$$

In equation (2) $v_{SM,x,y,z}$ is the voltage of one submodule in the respective converter arm, where every submodule has the same voltage due to the equal energy distribution; n_{SM} is the number of submodules in one converter arm – including 10% redundant submodules – and C_{SM} is the submodule capacity.

III. Control Design

The VSC HVDC control system is divided into two parts: The so called grid controller or P/Q, V_{DC}/Q controller and the energy/balancing controller. Their structure and control design is described in section III.A and III.B respectively. The grid controller is responsible for controlling the exchanged active and reactive power at the connected AC grids. The energy/balancing controller has to guarantee the right amount and distribution of energy in the converter and in-between the converter arms respectively.

Therefore, the output signals of the different controllers have to be superimposed in order to achieve the appropriate control signals for the controlled voltage sources in the upper and lower converter arm. The superposition is illustrated in Figure 3. As the grid and DC voltage controller are realized in the d/q/0 frame and the energy/balancing controller in the α/β/0 frame, an additional transformation from d/q/0 to α/β/0 is required.

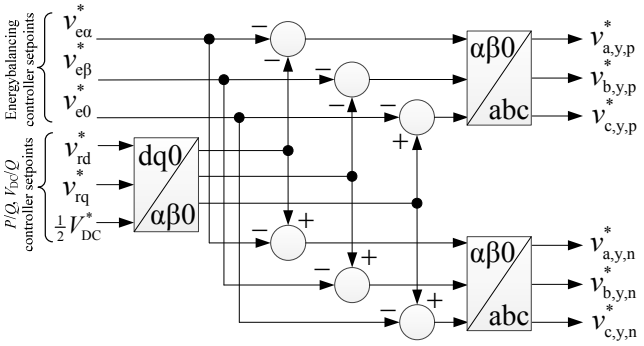

Figure 3: Superposition of the output signals of the P/Q, V_{DC}/Q and the energy/balancing controllers

A. Grid and DC Voltage Control

The grid and DC voltage control guarantees the exchange of the right amount of active and reactive power with the connected AC grid. As only one of the converters is able to

control the exchanged active power, the remaining converter controls the DC voltage of the system. The basic structure of the cascaded control system is illustrated in Figure 4. The subordinated current control loop uses a decoupling structure, which results from the coupling terms of the MMC in the d/q frame, see [10] and [16].

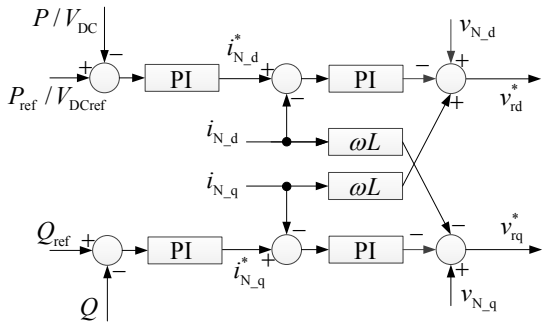

Figure 4: Cascaded control structure of the P/Q or V_{DC}/Q controller respectively and subordinated current controller in d/q frame

In order to apply a proper control design, the system has to be analyzed sufficiently. Detailed modeling of the MMC VSC HVDC system concerning grid control was done in [17]. Due to the decoupling terms in the control structure, the transfer function of the inner controlled system reveals as a concatenation of two first-order delays, shown in Figure 5, where T_A is the dead time of one calculation cycle, $R = R_N + R_{arm}/2$ and $L = L_N + L_{arm}/2$:

$$F_i(s) = \frac{i_{N\_d/q}(s)}{v^*_{rd/q}(s)} = \frac{1}{1+T_A s} \cdot \frac{1/R}{1+\frac{L}{R}s}. \quad (3)$$

Applying PI-controllers to this system, control design can be based on the approach of amplitude optimum, a sophisticated optimization approach for subordinated control loops with a big and a small, not compensable time constant, which corresponds to the already mentioned dead time T_A. In this case, the dead time element was linearized by Taylor series decomposition and reveals in a first-order delay element.

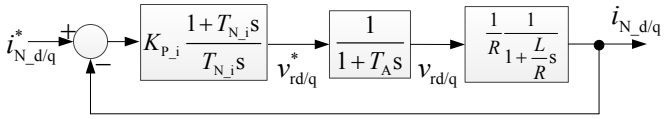

Figure 5: Block diagram of the inner current control loops in the d/q frame

The derivation of the appropriate controller gain and time constant for the approach of amplitude optimum might be found in [18]:

$$K_{P\_i} = \frac{T_{S\_i}}{2V_{S\_i}T_A} = \frac{L}{2T_A}, \text{ where } T_{S\_i} = \frac{L}{R},\ V_{S\_i} = \frac{1}{R}, \quad (4)$$

$$T_{N\_i} = T_{S\_i} = \frac{L}{R}. \quad (5)$$

Hence, the transfer function of the open inner control loop results in equation (6).

$$F_{oi}(s) = \frac{1}{2T_A s} \cdot \frac{1}{1+T_A s} \quad (6)$$

And the transfer function of the closed inner control loop can be stated:

$$F_{wi}(s) = \frac{1}{1+F_{oi}^{-1}(s)} = \frac{1}{1+T_o s+\frac{T_o^2}{2}s^2}, \text{ where } T_o = 2T_A, \quad (7)$$

as well as the open loop transfer function of the controlled system for the superimposed controller:

$$F_o(s) = \frac{P/Q(s)}{i^*_{N\_d/q}(s)} = \frac{\frac{3}{2}v_{N\_d}}{1+T_o s+\frac{T_o^2}{2}s^2} \approx \frac{\frac{3}{2}v_{N\_d}}{1+T_o s}. \quad (8)$$

The control structure of the outer active and reactive power control loop is shown in the following Figure.

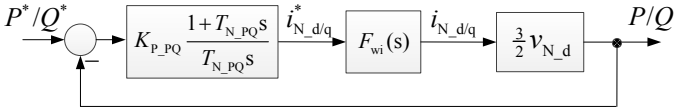

Figure 6: Block diagram of the outer power control loops

The outer power controllers are supposed to be significantly slower than the inner current control loops. Hence, the controller time constant can be chosen at least ten times slower than the subordinated current control loop [19]. The controller gain is determined according to the approach of amplitude optimum:

$$K_{P\_PQ} = \left(\frac{3}{2}\left|v^*_{N\_d}\right|\right)^{-1}, \quad (9)$$

$$T_{N\_PQ} = 10T_o. \quad (10)$$

The next step is the determination of the parameters for the V_{DC}/Q controller. Therefore, an expression for the dynamics of the DC voltage and the direct axis current can be derived by applying Kirchhoff's Current Law to the equivalent capacitor node:

$$i_C(t) = I_{DC1} - I_{DC2}. \quad (11)$$

The equivalent capacity is defined in equation (12); it contains the DC line capacity and an equivalent submodule capacity, which comprises six parallel converter arms, where each converter arm consists of a series connection of n_{SM} submodules:

$$C = C_{DC} + C_{eq} = C_{DC} + \frac{6C_{SM}}{n_{SM}}. \quad (12)$$

As the rectifier of the HVDC system is in active power control mode and taking the power balance at the inverter side into account, one can derive:

$$C\frac{dV_{DC2}}{dt} = I_{DC1} - \frac{3}{2}\frac{v_{N2\_d}}{V_{DC2}}i_{N2\_d}. \quad (13)$$

This differential equation is non-linear. Therefore, Taylor series decomposition around a steady state reference point is applied. To simplify the expression and to enable a linear control approach, solely the dependency of direct axis current is taken into consideration:

$$C\frac{d\Delta V_{DC2}}{dt} = -\frac{3}{2}\frac{v^*_{N2\_d}}{V^*_{DC2}}\Delta i_{N2\_d}. \quad (14)$$

Applying the Laplace transformation yields:

$$\frac{\Delta V_{\mathrm{DC2}}(\mathrm{s})}{\Delta i_{\mathrm{N2\_d}}(\mathrm{s})} = -\frac{3}{2}\frac{v^{*}_{\mathrm{N2\_d}}}{V^{*}_{\mathrm{DC2}}}\frac{1}{\mathrm{s}\,C}. \tag{15}$$

Hence, the parameters for the DC voltage controller can be derived using the approach of symmetrical optimum [18]; a sophisticated optimization approach for systems with an integral characteristic, where also the small, not compensable time constant T_{A} has to be considered:

$$K_{\mathrm{P\_DC}} = \frac{2V^{*}_{\mathrm{DC2}}C}{3v_{\mathrm{N2\_d}}2T_{\mathrm{A}}}. \tag{16}$$

To ensure stable operation of the DC voltage controller and to minimize controller interactions, the dead time and the filter time constant of the energy balancing controller have to be taken into account, since the DC voltage is correlated to the submodule voltages and the total energy, stored in the converter. Thus, the time constant of the DC voltage controller is composed:

$$T_{\mathrm{N\_DC}} = 4\left(T_{\mathrm{A}} + T_{\mathrm{filter\_1f}}\right) \approx 4T_{\mathrm{filter\_1f}}. \tag{17}$$

Accordingly, the control structure of the DC voltage control loop reveals as shown in the following Figure.

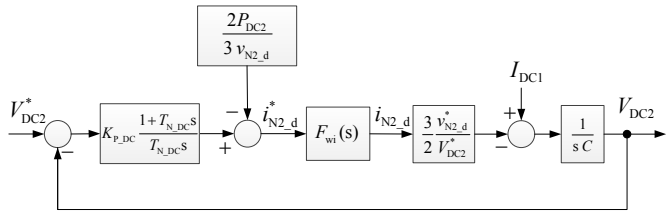

Figure 7: Block diagram of the DC voltage control loop

B. Energy Control – Cascaded Energy-, Horizontal and Vertical Balancing Control

In order to ensure a stable converter operation and to minimize submodule capacitor voltage fluctuations, the stored energy in the six converter arms has to be kept at a constant level. Furthermore, the energy between each phase of the converter has to be balanced and energy differences between the upper and lower arms of each phase are controlled to zero, in order to minimize fluctuations and distortions of the submodule voltages.

A cascaded control approach similar to [20] and [21] is carried out. Due to the MMC topology, so called circulating currents occur in the converter and distort the capacitor voltages of the submodules. These currents can be described as the arithmetic mean value of the currents in the upper and lower arm of each phase:

$$i_{\mathrm{diff,x}} = \frac{1}{2}\left(i_{\mathrm{x,p}} + i_{\mathrm{x,n}}\right). \tag{18}$$

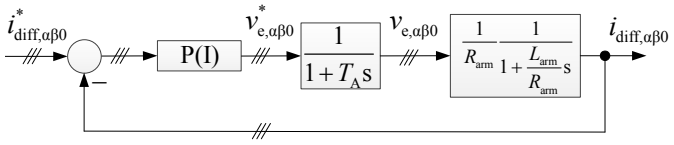

Figure 8: Block diagram of the inner current control loop in α/β/0 frame

As shown in Figure 8, the subordinated circulating current controller is designed in the α/β/0 reference frame. While the outer energy/balancing controllers ensure zero steady state error, it is sufficient to deploy a proportional controller in the inner current control loop. Nevertheless, it might be reasonable to include an integrator for the 0-component to achieve enhanced dynamic performance.

The controllers have to provide a robust behavior and have to track the current reference values very fast. Thus, the approach of amplitude optimum can be used here too. Taking the dead time of one calculation cycle T_{A} into account, the controller gain can be determined:

$$K_{\mathrm{P\_idiff}} = \frac{T_{\mathrm{S\_idiff}}}{2V_{\mathrm{S\_idiff}}T_{\mathrm{A}}}, \tag{19}$$

$$\text{where } T_{\mathrm{S\_idiff}} = \frac{L_{\mathrm{arm}}}{R_{\mathrm{arm}}} \text{ and } V_{\mathrm{S\_idiff}} = \frac{1}{R_{\mathrm{arm}}},$$

$$T_{\mathrm{N\_idiff}} = T_{\mathrm{S\_idiff}} = \frac{L_{\mathrm{arm}}}{R_{\mathrm{arm}}}. \tag{20}$$

Since the filter time constant of the superordinated energy and balancing controllers $T_{\mathrm{filter\_1f}}$ has to be considered too, the dead time can be neglected, since it is much smaller than the filter time constant:

$$K_{\mathrm{P\_idiff}} = \frac{L_{\mathrm{arm}}}{2T_{\mathrm{filter\_1f}}}. \tag{21}$$

Hence, the transfer function of the open inner control loop reveals in the following equation:

$$F_{\mathrm{oidiff}}(\mathrm{s}) = \frac{1}{2T_{\mathrm{filter\_1f}}\mathrm{s} + 2T_{\mathrm{filter\_1f}}T_{\mathrm{A}}\mathrm{s}^{2}}. \tag{22}$$

And the transfer function of the closed inner control loop can be stated:

$$F_{\mathrm{widiff}}(\mathrm{s}) = \frac{1}{1+F^{-1}_{\mathrm{oidiff}}(\mathrm{s})} = \frac{1}{1+2T_{\mathrm{filter\_1f}}\mathrm{s}+2T_{\mathrm{filter\_1f}}T_{\mathrm{A}}\mathrm{s}^{2}}. \tag{23}$$

Neglecting the higher order terms, the simplified transfer function of the closed inner current control loop reveals in a first-order delay with a time constant of $2T_{\mathrm{filter\_1f}}$.

Figure 9 gives a detailed overview on the energy control loops including the horizontal and vertical balancing controllers. The active power $p_{\mathrm{x,z}}$ is obtained from the arm currents and arm voltages. To derive the submodule voltages, the energy model presented in equation (2) is applied and the sum and difference voltages reveal as depicted in equation (24) and (25), where $x \in \{\mathrm{a,b,c}\}$ and $z \in \{\mathrm{p,n}\}$.

$$v_{\mathrm{SM},\Sigma,x} = \frac{1}{2}\left(v_{\mathrm{SM},x,\mathrm{p}} + v_{\mathrm{SM},x,\mathrm{n}}\right) \tag{24}$$

$$v_{\mathrm{SM},\Delta,x} = v_{\mathrm{SM},x,\mathrm{p}} - v_{\mathrm{SM},x,\mathrm{n}} \tag{25}$$

The sum of the two arm voltages $v_{\mathrm{SM},\Sigma,x}$ defines the total amount of energy stored per phase, whereas their difference $v_{\mathrm{SM},\Delta,x}$ represents the vertical energy difference per phase. For stable converter operation, it is crucial to keep submodule capacitor voltages in a narrow band. In order to achieve rapid control response of the mean reference value, lowpass filters are used. While the set-point of the controller for the zero component $\overline{v}_{\mathrm{SM},\Sigma,0}$ is the desired submodule voltage $\overline{v}^{*}_{\mathrm{SM}}$, the

set-points of the controllers for the α/β-components $\overline{v}_{\mathrm{SM},\Sigma,\alpha\beta}$ are zero.

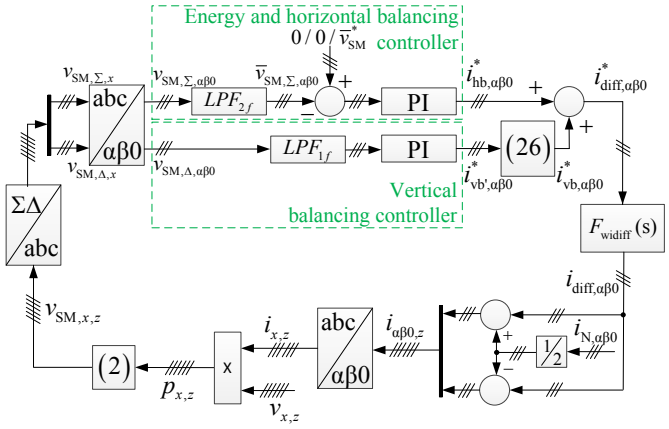

Figure 9: Block diagram of the energy-, horizontal- and vertical balancing control loop

Each of the respective energies per phase has to be varied to achieve horizontal balance; in order to avoid unsymmetrical line currents, as a result of changing the AC power in each phase, horizontal balance can be obtained by controlling the α/β-components of the inner current and thereby changing DC power per phase. Vertical balance is preserved by varying the phase power in an inhomogeneous manner; therefore, a negative sequence component of the inner current is introduced [22], [23]. As a result, only the active power in the respective phase is varied. This can be achieved by using the transformation of the following equation.

$$\mathbf{T}_{\alpha'\beta'0'/\alpha\beta0} = \begin{pmatrix} \cos(-\omega t) & \sin(-\omega t) & \cos(\omega t) \\ \sin(-\omega t) & -\cos(-\omega t) & \sin(\omega t) \\ 0 & 0 & 0 \end{pmatrix} \quad \text{(26)}$$

(Negative sequence sys. / Pos. seq. sys.)

It can be shown that the sum quantities contain a characteristic double line frequency component and their respective delta quantities a fundamental frequency component [20]. Therefore the deployed lowpass filters LPF_{1f} and LPF_{2f}, depicted in Figure 9, are realized as first-order delay blocks with the appropriate filter time constants:

$$T_{\mathrm{filter\_1f}} = 1/f_{\mathrm{N}}, \quad \text{(27)}$$

$$T_{\mathrm{filter\_2f}} = 1/(2f_{\mathrm{N}}). \quad \text{(28)}$$

For the calculation of the controller parameters, the equivalent time constant of the inner current control loop and the time constant of the lowpass filters have to be considered. The controller parameters for the energy/horizontal balancing controller and the vertical balancing controller can be derived using the approach of symmetrical optimum:

$$K_{\mathrm{P\_hb/0}} = \frac{1}{2V_{\mathrm{S\_idiff}}T_{\mathrm{res}}} = \frac{C_{\mathrm{SM}}}{4T_{\mathrm{filter\_2f}}}, \quad \text{where } V_{\mathrm{S\_idiff}} = \frac{1}{C_{\mathrm{SM}}} \text{ and } T_{\mathrm{res}} = 2\left(T_{\mathrm{A}} + T_{\mathrm{filter\_2f}}\right) \approx 2T_{\mathrm{filter\_2f}}, \quad \text{(29)}$$

$$T_{\mathrm{N\_hb/0}} = 4T_{\mathrm{filter\_2f}}, \quad \text{(30)}$$

$$K_{\mathrm{P\_vb}} = \frac{1}{2V_{\mathrm{S\_ie}}T_{\mathrm{res}}} = \frac{C_{\mathrm{SM}}}{4T_{\mathrm{filter\_1f}}}, \quad \text{where } V_{\mathrm{S\_ie}} = \frac{1}{C_{\mathrm{SM}}} \text{ and } T_{\mathrm{res}} = 2\left(T_{\mathrm{A}} + T_{\mathrm{filter\_1f}}\right) \approx 2T_{\mathrm{filter\_1f}}. \quad \text{(31)}$$

$$T_{\mathrm{N\_vb}} = 4T_{\mathrm{filter\_1f}}. \quad \text{(32)}$$

As the outer control loops perform different tasks, in terms of balancing, the reference values of the inner current controllers are superimposed. Therefore, the matrix of equation (26) has to be applied:

$$i^*_{\mathrm{diff},\alpha\beta0} = i^*_{\mathrm{vb},\alpha\beta0} + i^*_{\mathrm{hb},\alpha\beta0} = \mathbf{T}_{\alpha'\beta'0'/\alpha\beta0} i^*_{\mathrm{vb}',\alpha\beta0} + i^*_{\mathrm{hb},\alpha\beta0}. \quad \text{(33)}$$

IV. Results

The presented EMT model and its entire control system as described in the previous sections is implemented in MATLAB/Simulink® using the SimPowerSystems® toolbox.

In this chapter a start-up process of the HVDC system, a subsequent power reversal process and two AC voltage drops – at the connection points of the HVDC system – are presented.

A DC overhead line with a length of 300 km is assumed; the line parameters are selected according to [24]. Moreover, the values for the grounding impedances are proposed in [25]. General parameters of the HVDC system can be found in Table I and the control parameters, according to the outlined approaches, are given in Table II.

Table I: General HVDC parameters

Parameter	Value	Parameter	Value
T_{A}	10^{-4} s	C_{SM}	10 mF
$f_{\mathrm{N1}} = f_{\mathrm{N2}}$	50 Hz	n_{SM}	440
$V_{\mathrm{N1}} = V_{\mathrm{N2}}$	333 kV	V_{SM}	1.8 kV
$R_{\mathrm{N1}} = R_{\mathrm{N2}}$	0.19 Ω	l_{DC}	300 km
$L_{\mathrm{N1}} = L_{\mathrm{N2}}$	60.5 mH	R'_{DC}	0.0144 Ω/km
L_{arm}	50 mH	L'_{DC}	0.9536 mH/km
R_{arm}	1.57 Ω	C'_{DC}	12.3 nF/km
$L_{\mathrm{gnd\ AC1}} = L_{\mathrm{gnd\ AC1}}$	5000 H	$V_{\mathrm{DC\ ref}}$	640 kV
$R_{\mathrm{gnd\ AC1}} = R_{\mathrm{gnd\ AC2}}$	5 kΩ	$P_{\mathrm{ref\ N1/N2}}$	1000 MW
$R_{\mathrm{gnd\ DC1}} = R_{\mathrm{gnd\ DC1}}$	1 MΩ	$Q_{\mathrm{ref\ N1/N2}}$	-100/200 MVA

Table II: Controller parameters

Parameter	Value	Parameter	Value
$K_{\mathrm{p\ iN\ dq0}}$	285.0	$K_{\mathrm{p\ ie\ \alpha\beta}}$	5.0
$T_{\mathrm{N\ iN\ dq0}}$	87.7 ms	$K_{\mathrm{p\ ie\ 0\ PQ/DC}}$	500/5
$K_{\mathrm{p\ P}}$	$2.45 \cdot 10^{-6}$	$K_{\mathrm{p\ en\ PQ/DC}}$	1.00/1.35
$T_{\mathrm{N\ P}}$	2 ms	$T_{\mathrm{N\ en\ PQ/DC}}$	40 ms/21.9 ms
$K_{\mathrm{p\ Q}}$	$2.45 \cdot 10^{-6}$	$K_{\mathrm{p\ hb\ PQ/DC}}$	0.50/0.925
$T_{\mathrm{N\ Q}}$	2 ms	$T_{\mathrm{N\ hb\ PQ/DC}}$	40 ms/40 ms
$K_{\mathrm{p\ DC}}$	0.29	$K_{\mathrm{p\ vb\ PQ/DC}}$	1.00/1.85
$T_{\mathrm{N\ DC}}$	0.5 s	$T_{\mathrm{N\ vb\ PQ/DC}}$	80 ms/80 ms

A. Energization and Start-up

During the passive energization process all controllers are disabled and the converter is blocked. Pre-charging resistors are used with respect to the current limitation boundaries of the deployed IGBTs. The positive sequence voltages and currents of the AC grids are depicted in Figure 10. It can be

observed that the converters are charged passively via their adjacent AC grids. The submodule capacitor voltages in Figure 11 show that, as soon as the submodule capacitor voltages have reached $V_{DC\_N}/2n_{SM}$, the charging process stops and the pre-charging resistors can be bypassed.

The submodule voltage control of both converters is enabled at $t = 0.25$ s and the reference value is tracked fast and accurate; converter 1 is charged via the DC link with no additional power infeed from AC grid 1, which can be seen in Figure 12. The submodules of converter 2 are charged via AC grid 2, since the DC voltage controller, which is also enabled at $t = 0.25$ s, requires active power from AC grid 2 in order to keep the DC voltage at its desired level. The submodule voltages of both converters are increased to 1.8 kV. Simultaneously to the submodule capacitor voltages, the DC voltage is ramped up to its nominal value of 640 kV, as shown in Figure 13, with respect to the modulation index limitation.

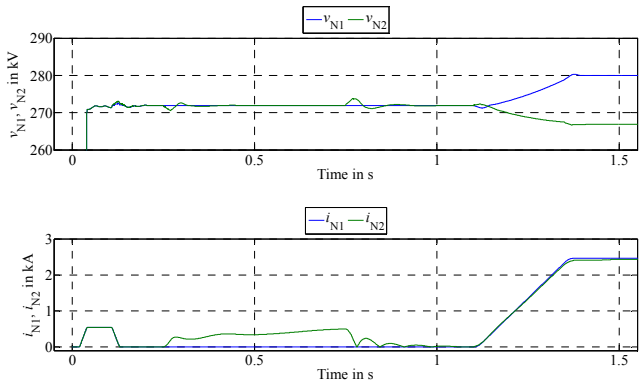

Figure 10: Energization and start-up – AC voltages & currents

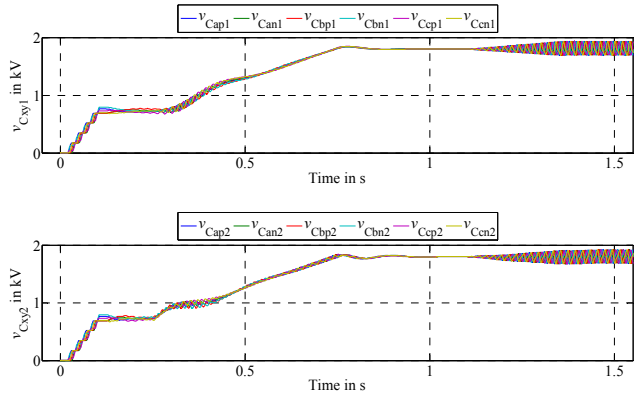

Figure 11: Energization and start-up – submodule voltages

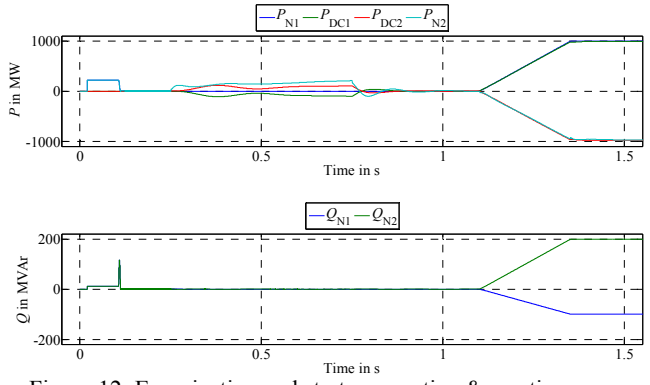

Figure 12: Energization and start-up – active & reactive power

As the converter energization is completed, the power controllers are enabled at $t = 1.1$ s, where the active power set-point is ramped up to 1000 MW within 0.25 s. The reactive power set-points are chosen independently to +200 MVA for the AC grid 2 sided converter and to -100 MVA for the AC grid 1 sided converter respectively. The actual values of the active and reactive power follow their set-points immediately. The AC voltages at the connection points of the converters increase and decrease dependent on the appropriate capacitive or inductive reactive power infeed.

Regarding the DC quantities, it can be deduced that the currents contain no AC components. The DC voltage is maintained at its reference value of 640 kV during the power ramp-up.

As soon as the power transmission is started, the submodule voltages show a characteristic spreading. Converter control is well designed to maintain submodule voltages in a narrow band of approximately 240V – dependent on the transmitted power.

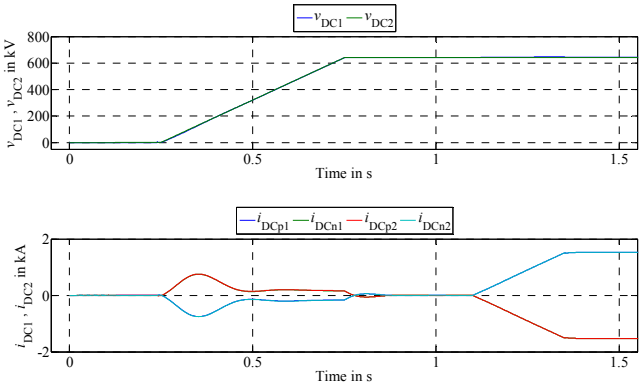

Figure 13: Energization and start-up – DC voltages & currents

B. Power Reversal and AC voltage drop

At $t = 1.6$ s a power reversal process is initialized, where the set-point of the active power controller is changed from 1000 MW to -1000 MW applying a 0.5 s ramp. Figure 14 shows that the actual values of the active power follows the set-point very accurately. The AC voltages, as illustrated in Figure 15, are slightly reduced during the power reversal; whereas the AC currents drop further down, but don't reach the zero line, since there is still a reactive power infeed into the AC grid, which is not affected. The spreading of the submodule voltages in Figure 16 narrows during the power reversal, since the active power decreases during a time span of 0.5 s, but is in the same range afterwards. The DC voltage of converter 1, depicted in Figure 17, changes according to the direction of the DC current and the appropriate voltage at the line impedance, since the DC voltage of converter 2 is kept constant.

Once the power reversal process is finished, a 20% voltage drop at the AC connection point of converter 2 occurs at $t = 2.3$ s and a subsequent 20% voltage drop in AC grid 1 at $t = 2.7$ s. Since the power transmission is maintained by the power controllers, the AC currents rise, once the voltage drops occur. The active and reactive power infeed is slightly distorted and return to their set-points very fast. The DC quantities show only small oscillations and keep almost constant. Since the AC currents are increased the spreading of the submodule voltage rises.

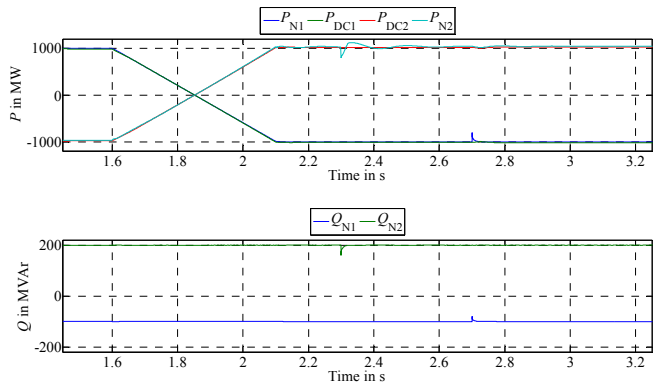

Figure 14: Power reversal and voltage drop – active & reactive power

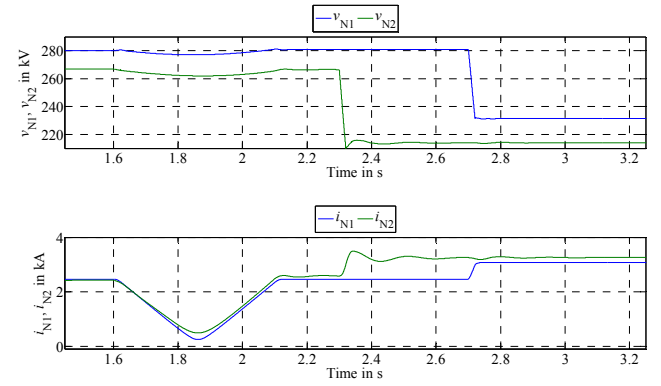

Figure 15: Power reversal and voltage drop – AC voltages & currents

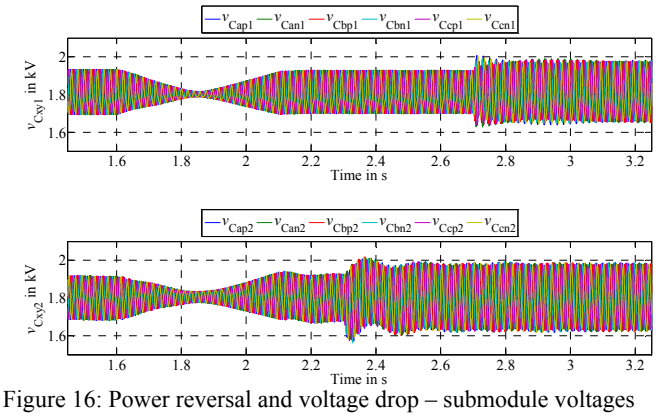

Figure 16: Power reversal and voltage drop – submodule voltages

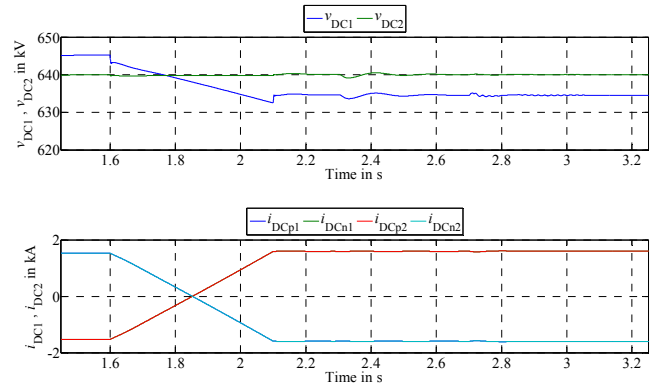

Figure 17: Power reversal and voltage drop – DC voltages & currents

V. Conclusion

A detailed model of a Modular Multilevel Converter based VSC HVDC System and its entire cascaded control scheme – consisting of the P/Q and V_{DC}/Q controller with a subordinated current control loop in the d/q frame, as well as an energy/balancing controller with a subordinated current control loop in the α/β/0 frame – has been proposed.

Control design has been carried out for all controllers according to the outlined optimization approaches of amplitude optimum or symmetrical optimum respectively. The interactions of the inner balancing controllers and the V_{DC} controller were revealed.

An energization, a start-up and a power reversal process of the HVDC system is presented and the dynamic behavior is analyzed. The results highlight the stability and robustness of the proposed control system and showed that the used control design approaches guarantee a stable operation of the entire HVDC system. Even in the case of two subsequent 20% voltage drops in the respective AC grids, the control system shows a very stable behavior and guarantees the desired transmission of active power and a constant reactive power infeed.

The proposed model with the appropriate control scheme might be used for EMT HVDC studies; it is implemented in MATLAB/Simulink® and could be easily converted to other simulation tools.

References

[1] A. Lesnicar and R. Marquardt, "An innovative modular multilevel converter topology suitable for a wide power range," in *Proc. IEEE PowerTech*, pp. 272–277, Bologna, June 2003.

[2] 50Hz, Amprion, TenneT, TransnetBW – TSO's of Germany, "Grid development plan – 2nd draft" (Netzwentwicklungsplan Strom - 2. Entwurf), 2014.

[3] ENTSO-E, "Ten Year Network Development Plan", 2014.

[4] J. Dorn, H. Huang and D. Retzmann, "A New Multilevel Voltage-Sourced Converter Topology for HVDC Applications," in *Proc. Cigre Session*, B4-304, Paris, 2008.

[5] M. Dommaschk, *Modular multilevel converters for HVDC applications (Modularer Multilevelstromrichter fuer Anwendungen in der Hochspannungsgleichstrombertragung)*. Göttingen: Cuvillier Publishing, 2013.

[6] M. Saeedifard and R. Iravani, "Dynamic performance of a modular multilevel back-to-back HVDC system," *IEEE Trans. Power Del.*, vol. 25, no. 4, pp. 2903-2912, Oct. 2010.

[7] J. Peralta, H. Saad, S. Dennetière, J. Mahseredjian and S. Nguefeu, "Detailed and averaged models for a 401-level MMC-HVDC system," *IEEE Trans. Power Delivery*, vol. 27, no. 3, pp. 1501-1508, Jul. 2012.

[8] S. Dennetière, H. Nguefeu, H. Saad and J. Mahseredjian, "Modeling of modular multilevel converters for the France-Spain link," in *Proc. Int. Conf. Power System Transients*, Vancouver, July 2013.

[9] A. Beddard, M. Barnes and R. Preece, "Comparison of Detailed Modeling Techniques for MMC Employed on VSC-HVDC Schemes," *IEEE Trans. Power Delivery*, vol. 30, no. 2, pp. 579-589, June 2015.

[10] A. Antonopoulos, L. Angquist and H.-P. Nee, "On Dynamics and Voltage Control of the Modular Multilevel Converter," in *Proc. European Conf. Power Electronics and Applications (EPE)*, pp. 1-10, Barcelona, Sept. 2009.

[11] G. Bergna, E. Berne, P. Egrot, P. Lefranc, A. Arzande, J.-C. Vannier and M. Molinas, "An energy-based controller for HVDC modular multilevel converter in decoupled double synchronous reference frame for voltage oscillation reduction," *IEEE Trans. Industry Applications*, vol. 60, no. 6, pp. 2360-2371, Jun. 2013.

[12] H.Saad, X. Guillaud, J. Mahseredjian, S. Dennetiere and S. Nguefeu, "MMC Capacitor Voltage Decoupling and Balancing Controls," *IEEE Trans. Power Delivery*, vol. 30, no. 2, pp.704-712, April 2015.

[13] M. K. Bucher, R. Wiget, G. Andersson and C. M. Franck, "Multi-Terminal HVDC Networks - What is the Preferred Topology?," *IEEE Trans. Power Delivery*, vol. 29, no. 1, pp. 406-413, Feb. 2014.

[14] S. Debnath Q. Jiangchao, B. Bahrani, M. Saeedifard and P. Barbosa, "Operation, Control, and Applications of the Modular Multilevel Converter: A Review," *IEEE Trans. Power Electronics*, vol. 30, no. 1, pp. 37-53, Jan. 2015.

[15] M. Lehmann, C. Hahn and M. Luther, "A Novel Approach for Energy Balanced Operation of Submodules in Multilevel VSC HVDC Systems," in *Proc. Universities Power Engineering Conference (UPEC)*, Staffordshire, Sept. 2015.

[16] Q. Tu, Z. Xu, Y. Chang and L. Guan, "Suppressing dc voltage ripples of MMC-HVDC under unbalanced grid conditions," *IEEE Trans. Power Delivery*, vol. 27, no. 3, pp. 1332–1338, July 2012.
[17] C. Hahn, M. Burkhardt, A. Semerow, M. Luther and O. Ruhle, "Generic modeling of a self-commutated multilevel VSC HVDC system for power system stability studies," in *Proc. Applied Power Electronics Conference and Exposition (APEC)*, pp. 2672-2677, Charlotte, March 2015.
[18] D. Schröder, *Electric drives – Control of drive systems (Elektrische Antriebe – Regelung von Antriebssystemen)*. New York: Springer Publishing, 2009.
[19] F. Martinez-Rodrigo, S. de Pablo and L. Carlos Herrero-de Lucas, "Current control of a modular multilevel converter for HVDC applications," *Elsevier Renewable Energy Journal*, vol. 38, no. 1, pp. 318-338, Nov. 2015.
[20] J. Kolb, *Optimized Operation of the modular multilevel converter for drive systems" (Optimale Betriebsführung des Modularen Multilevel-Umrichters als Antriebsumrichter für Drehstrommaschinen)*. Karlsruhe: KIT Scientific Publishing, 2014.
[21] J. Kolb, F. Kammerer and M. Braun, "Straight forward vector control of the Modular Multilevel Converter for feeding three-phase machines over their complete frequency range," in *Proc. 37th Annu. Conf. IEEE Ind. Electron. Soc.*, pp. 1596-1601, Melbourne, Nov. 2011.
[22] P. Münch, *Conception and Design of an integrated control for MMCs (Konzeption und Entwurf integrierter Regelungen für Modulare Multilevel Umrichter)*. Berlin: Logos Publishing 2010.
[23] P. Münch, D. Gorges, M. Izak and S. Liu, "Integrated current control, energy control and energy balancing of Modular Multilevel Converters," in *Proc. 36th Annu. Conf. IEEE Ind. Electron. Soc.*, pp. 150–155, Glendale, Nov. 2010.
[24] Cigré Working Group B4-57, "Guide for the Development of Models for HVDC Converters in a HVDC Grid", Cigré Tech. Rep. 604, Dec. 2014.
[25] M. K. Bucher and C. M. Franck, "Comparison of fault currents in multiterminal HVDC grids with different grounding schemes," in *Proc. IEEE PES General Meeting Conf. and Exp.*, pp. 1-5, National Harbor, July 2014.

BIOGRAPHIES

Christoph Hahn (M'2012) received his Dipl.-Ing. degree from the University of Erlangen-Nuremberg, Germany, in 2011. Currently he is research associate and working towards a Ph.D. at the Institute of Electrical Energy Systems at the University of Erlangen-Nuremberg, Germany. His research interests lie in the field of HVDC modeling and control.

Matthias Burkhardt received his B.Sc. and M.Sc. degree from the University of Erlangen-Nuremberg, Germany, in 2013 and 2016 respectively. His research interests lie in the field of HVDC & FACTS applications and the development of HVDC-MT concepts.

Matthias Luther (M'2011) studied electrical engineering and received his Ph.D. at the Technical University of Brunswig, Germany in 1992. From 1993 he held different functions and management positions in the electricity industry at PreussenElektra, E.ON Netz and TenneT TSO. Since 2011 he is professor and is head of the Institute of Electrical Energy Systems at the University of Erlangen-Nuremberg, Germany.